

FULL PAPER

Influence of reducing agents in nanoparticle synthesis: SnO₂-ZnO composite anode

D. Lakshmi^{1,2} | M. Infanta Diana¹ | Gayathri Manoj¹ | S. Jayapandi³ |
B. Nalini⁴ | P. Christopher Selvin¹ | P. Balraju⁵

¹LSSI lab, Department of Physics, Bharathiar University, Coimbatore, India

²Department of Physics, PSG College of Arts and Science, Coimbatore, India

³Department of Physics, SSN College of Engineering, Chennai, India

⁴Department of Physics, Avinashilingam Institute for Home Science and Higher Education for Women, Coimbatore, India

⁵Department of Physics, Coimbatore Institute of Technology, Coimbatore, India

Correspondence

P. Christopher Selvin, LSSI lab, Department of Physics, Bharathiar University, Coimbatore, India.
Email: cphysics@buc.edu.in

Funding information

Council of Scientific and Industrial Research (CSIR), India, Grant/Award Number: 09/472(0189)/219-EMR-I

Abstract

The present research work is dedicated to understand the effect of synthesis medium on the nanocomposite anode, SnO₂: ZnO, and their synergistic effects towards Li-ion battery applications. Alkaline and acidic media as reducing agents such as NaOH, LiOH, and NaBH₄ are chosen for the preparation of the composite, and the results are surprisingly varying. Structural analysis by means of X-ray diffraction shows the mixed crystal symmetry inclusive of SnO₂ and ZnO phases for all the three systems with varying ranges of each phases. The average crystallite sizes are around 20–39 nm for all the three samples. Morphological analysis of SnO₂: ZnO anode by means of transmission electron microscopy indicates mixed shapes of grains for the samples synthesized by NaOH and LiOH, whereas reducing agent, NaBH₄, falls into the spherical shape predominantly. Raman and selected area electron diffraction analyses validate the mixed crystal symmetry of all the three samples. Electrochemical performance of the samples is promising where NaBH₄ mediated anode delivers reversible capacity around 225 m Ahg⁻¹ exclusively. In the aspect of electrical conductivity, almost all the three samples employed with three different reducing agents fall in the range of $\sim 10^{-4}$ S cm⁻¹ at room temperature, validating the choice of the material as anode in Li-ion battery technology.

KEYWORDS

anode, charge–discharge analysis, impedance, Raman, reducing agents

1 | INTRODUCTION

Since the discovery, the growth and development curve of Li-ion batteries and their components never flattened due to the pervasive applications of these devices in a commercial venture. The growing markets and consumer needs require exploration of newer kinds of components as battery candidates to improve the safety and performance of the devices. Other than the most reliable carbon-based anodes, Li-ion conducting

intercalation/conversion type anodes, such as metal-based alloys, nitrides, phosphides, and metal oxides, are extensively analyzed.^[1–3] One of the interesting properties of the metal oxide class is their ability to integrate into different alloys by incorporation of any kind of foreign elements in their crystal structure based on the application area. Inter-metallic compounds (Ni, Fe, V, Mn, Ti, Sb, and Ge based anodes) transition metal oxides based conversion/alloying type anodes, and metal-organic framework-derived anodes

are the advanced anode materials in current practice.^[4-6]

Tin oxide is one of the metal oxide kinds of anodes that attained deep research attention and explored extensively. Among different phases, SnO₂ is the most stable phase of this metal that possesses a high theoretical capacity (~1494 mAh g⁻¹) and great stability over high numbers of cycles.^[7,8] Tin oxide undergoes three steps of redox reactions which include conversion and alloy types. During conversion reaction, SnO₂ transfers into SnO and then into Sn element which induces much structural stress and volumetric collapse into the crystal structure on repeated cycles.^[9] Such a happening is highly unwanted in a good performing anode materials. To attempt this limitation, stability boosters such as the addition of buffer elements, carbon inclusion, and protective coatings are proposed widely.^[10] Looking into this, protective coatings by means of metal oxides can be a wise choice as metal oxides can also involve in the redox activity of the host at controlled steps.

Modification of SnO₂ by Zn or ZnO is a great combo in this viewpoint as Zn and Sn both possess similar structural and electrochemical properties, phase formation ability with Li, and good electrical conductivity. Although SnO₂-ZnO pair has been investigated widely,^[11-14] its battery perspectives have to be explored further to understand both the success and stopping parameters of this particular combination for practical applications. ZnO is also an active component in lithium ion battery aspects which possess a theoretical capacity of 987 mAh g⁻¹.^[15] The addition of this phase into SnO₂ will be highly beneficial due to the proven success of this combination than the pristine phase of their individuals. Here SnO₂ and ZnO exhibit redox reactions at separate voltages, so that they both can act as a mutual buffer to each other.

Zn-SnO₂ can be easily achieved via the co-precipitation method with simple steps of preparation. Although overall properties of any anode is material dependent, particle morphology, crystal symmetry, particle size, and elemental composition are the crucial but silent parameters that determine the efficacy of the materials for target applications. In this purview, a significant and new attempt has been made to explore the effect of reducing agents on the phase forming ability and their impact on physico-electrochemical aspects of the materials. For this purpose, NaOH, LiOH, and NaBH₄ are chosen as reducing agents, and their effect on different properties of SnO₂-ZnO is studied. In this work, Zn is introduced as a dopant in the SnO₂ matrix, but partial occupancy of Zn in the Sn sites and complete ZnO phase formation along with SnO₂

phase—both are probable and allowed to exist for better battery aspects of them.

2 | EXPERIMENTAL SECTION

2.1 | Materials and synthesis

Zinc-stannic oxide powder is prepared by the simple co-precipitation method. Equimolar ration of metal chlorides (SnCl₂·2H₂O, ZnCl₂) are taken where the collective weight of the metal salts is 1.7 g and dissolved in 50 mL of distilled water. After thorough mixing, the prepared solution is reduced by various reducing agents, viz. NaOH, LiOH, and NaBH₄ by maintaining pH at 8. The solution is vigorously stirred for 3 h until precipitation. After 20 min of aging, the precipitates are filtered and washed with distilled water and ethanol followed by drying at 80 °C for 12 h. The dried powders are ground well and calcined at 800 °C for 3 h. The obtained white powders are stored and used for further analysis. Hereafter, the powders prepared by NaOH, LiOH, and NaBH₄ are specified as Sn_{0.5}Zn_{0.5}O₂-A, Sn_{0.5}Zn_{0.5}O₂-B, and Sn_{0.5}Zn_{0.5}O₂-C, respectively.

2.2 | Instrumentations

All the samples prepared in the research work are analyzed for structural properties (X ray diffraction analysis [XRD, Panalytical X-pert pro-Cu K_α]), morphological-selected area electron diffraction (SAED; transmission electron microscopy-TEM, FEI Tecnai G2 20 S-TWIN TEM), elemental compositional (Energy Dispersive X-ray analysis [EDX] [TESCAN VEGA3 SBH]), Raman (WiTec alpha 300, Germany), electrochemical, and AC impedance (cyclic voltammetry [CV] and charge-discharge analysis, Bio-Logic SP 150) studies.

For AC impedance analysis, the Zn_{0.5}Sn_{0.5}O₂ samples are prepared as pellets (1 cm diameter and 1 mm thickness) using a hydraulic press and coated with Ag paste for electrical contact. For CV measurements, the Zn_{0.5}Sn_{0.5}O₂ samples are cast on Cu foil using active material, acetylene black, and PVdF binder in the weight ratio of 75:15:10, and slurry is prepared using N-methyl-2-pyrrolidone solvent. The obtained foils are dried at 100 °C for 12 h in a vacuum. Three-electrode setup is preferred employing foils of zinc-stannic oxides as working electrode, Ag/AgCl as reference electrode, and Pt wire as a counter electrode. 0.5 M aqueous LiOH is served as the electrolyte solution.

3 | RESULTS AND DISCUSSION

3.1 | XRD analysis

The XRD pattern observed for $\text{Zn}_{0.5}\text{Sn}_{0.5}\text{O}_2$ prepared with different reducing agents (NaOH, LiOH, and NaBH_4) are presented in Figure 1. Phase formation of SnO_2 is ascertained by characteristic diffraction planes of this material, and a well match is observed with JCPDS data (41–1445). The SnO_2 sample synthesized here possesses a tetragonal phase with $P_{42/mnm}$ symmetry. In addition to SnO_2 phase, a few planes associated with the ZnO phase is also observed in the resultant pattern at 32° , 34.5° , 36.5° , 48° , 57° , and 68° positions. The intensity of these planes varies in all three samples, perhaps the effect of the synthesis medium. The corresponding peak positions are marked in the XRD pattern (Figure 1).

For the reader's convention, the XRD pattern of pristine SnO_2 is also provided in Figure 1. Comparatively, the prominent peaks of SnO_2 get shifted to higher/lower angles on different reducing agents. The shifting of peaks confirms the incorporation of Zn dopants on Sn site without changing the crystal symmetry of SnO_2 . At selective positions, the diffraction peaks of stannic oxide are less intense than the ZnO phase for LiOH and NaBH_4 reducing agents. Especially, NaBH_4 promotes ZnO phase along with SnO_2 phase, which can be seen from the high intense (100) and (002) planes of ZnO. Further, the peaks of tin oxide get weaker gradually with LiOH and NaBH_4 synthesis media. Comparative percentages of SnO_2 and ZnO phases in all the three $\text{Zn}_{0.5}\text{Sn}_{0.5}\text{O}_2$ samples are listed in Table 1.

Rietveld refinement is carried out for all the three XRD patterns, and these findings are also given in Table 1. For

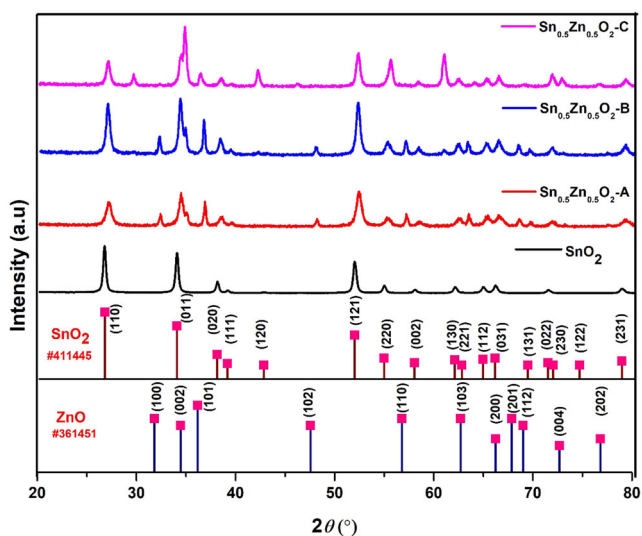


FIGURE 1 XRD patterns of $\text{Sn}_{0.5}\text{Zn}_{0.5}\text{O}_2$ samples

TABLE 1 Lattice parameters for $\text{Sn}_{0.5}\text{Zn}_{0.5}\text{O}_2$ samples

	Lattice constant (Å)			Volume ($\times 10^6 \text{ pm}^3$)	Crystallite size (nm)	Dislocation density δ (lines m^{-2})	Strain ϵ	WH plot		% Phase	
	a = b	c	c/a					Crystallite Size (nm)	Strain	SnO_2	ZnO
Standard value	4.73	3.18	0.6726	71.55	--	--	--	--	--	--	--
$\text{Sn}_{0.5}\text{Zn}_{0.5}\text{O}_2$ -A	4.68	3.16	0.6755	69.42	19.66	3.8×10^{15}	0.0049	0.0013	34.66	68.04	31.60
$\text{Sn}_{0.5}\text{Zn}_{0.5}\text{O}_2$ -B	4.70	3.17	0.6744	70.29	26.13	2.1×10^{15}	0.0036	0.0020	55.46	70.00	30.00
$\text{Sn}_{0.5}\text{Zn}_{0.5}\text{O}_2$ -C	4.69	3.16	0.6735	69.83	20.81	2.4×10^{15}	0.0043	0.0016	43.60	82.35	17.65

simplicity, XRD pattern refined for NaBH_4 system alone is shown in Figure 2. Different synthesis media or reducing agents employed in the co-precipitation method be critical factor influencing the crystallite size, lattice strain, morphology, and electrochemical performance.^[16] In this row, the peak shift towards a higher angle decreases the lattice constant “ a ” which decreases the volume of the unit cell. The lattice parameters, c/a ratio, and volume of $\text{Sn}_{0.5}\text{Zn}_{0.5}\text{O}_2$ unit cell prepared with different reducing agents show negligible variation, which is presented in Table 1. Further, an illustrative crystal structure is generated out of refinement parameters for NaBH_4 system, and the same is shown in Figure 3.

The crystallite sizes of the $\text{Sn}_{0.5}\text{Zn}_{0.5}\text{O}_2$ samples prepared at different synthesis mediums are calculated by Debye Scherer's equation¹⁷. Remarkably, all three samples deliver three different crystallite sizes as mentioned here: $\text{Sn}_{0.5}\text{Zn}_{0.5}\text{O}_2$ -A: 19 nm, $\text{Sn}_{0.5}\text{Zn}_{0.5}\text{O}_2$ -B: 26 nm, and $\text{Sn}_{0.5}\text{Zn}_{0.5}\text{O}_2$ -C: 20 nm and pristine SnO_2 : 39 nm. Size

reduction observed in the doped sample compared to the pure SnO_2 is the effect of Zn dopant here. Still, the addition of Zn into SnO_2 matrix induces peak shift and broadening as well. In addition to this, synthesis medium in the aspects of reducing agents also imposes lattice distortion, peak broadening, and lattice strain. Primarily, lattice strain (ϵ) and dislocation density (δ) are calculated by the following formulae^[18];

$$\epsilon = \beta \tan \theta \quad (1)$$

$$\delta = \frac{1}{D^2} \text{ lines m}^{-2} \quad (2)$$

where

β is the full width at half maximum (rad),
 δ is the dislocation density (dislocations cm^{-2}), and
 D is the crystallite size (nm).

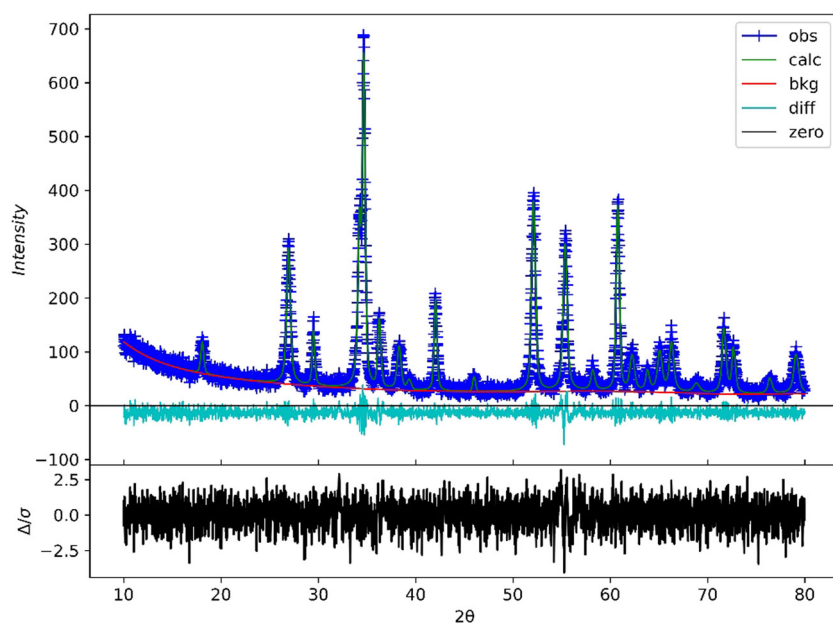


FIGURE 2 Rietveld refined XRD pattern of SnO_2 : ZnO sample (prepared by NaBH_4)

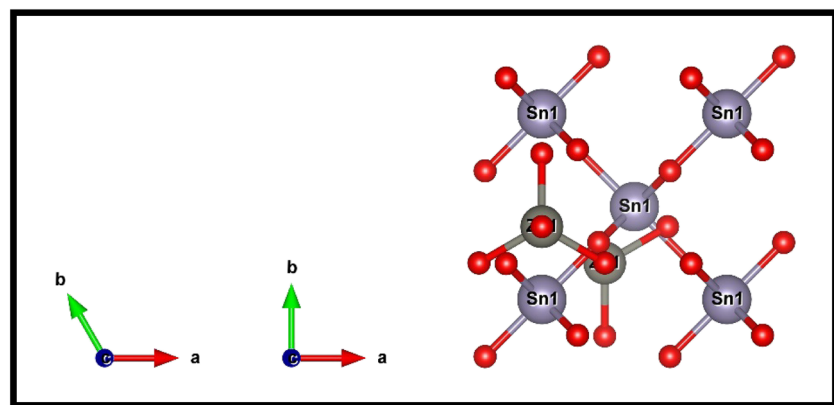


FIGURE 3 Crystal structure of SnO_2 : $\text{ZnO}/\text{Sn}_{0.5}\text{Zn}_{0.5}\text{O}_2$ composite

The findings are listed in Table 1. To verify the cause of peak broadening in all three samples, Williamson-hall (WH) plot method is employed (Figure 4). From the plot, it is ensured that both the size and strain parameters cause peak broadening in $\text{Sn}_{0.5}\text{Zn}_{0.5}\text{O}_2$ samples. From the liner fitting, it is observed that the strain values are similar for NaOH and NaBH_4 samples, whereas sample synthesized using LiOH shows slight disparity. Similarly, the crystallite size of the sample synthesized using LiOH is larger compared to the other two, as calculated from the WH plot.

Dislocation density is the parameter that describes if any anomaly from an ideal diffraction pattern exists. When an atom in crystal unit cells is displaced from their ideal position due to small crystallite and lattice defects, the broadening of the peaks occur. From the findings, it is concluded that as the crystallite size increases, dislocation density decreases. Sample synthesized by LiOH falls into the lowest δ value, whereas the other two samples fall into 2.4×10^{15} ($\text{Sn}_{0.5}\text{Zn}_{0.5}\text{O}_2\text{-C}$) and 3.8×10^{15} ($\text{Sn}_{0.5}\text{Zn}_{0.5}\text{O}_2\text{-A}$).

3.2 | Raman analysis

Complete Raman analysis of the $\text{Sn}_{0.5}\text{Zn}_{0.5}\text{O}_2$ sample prepared by NaOH, LiOH, and NaBH_4 is shown in Figure 5. As seen in this Raman spectra, seven peaks are clearly seen in the A and B samples, whereas only four peaks are seen in the C sample. For rutile structures, out of 18 modes, only four (optical modes) are Raman active, viz. A_{1g} , B_{1g} , B_{2g} , and E_g .^[19] All these modes are observed

in the present Raman spectrum at $\sim 380\text{ cm}^{-1}$, 440 cm^{-1} , 635 cm^{-1} , and 776 cm^{-1} , respectively, which ensures the rutile SnO_2 of tetragonal symmetry. Raman analysis is completely crystallite size dependent that modifies the interaction of modes of vibration of the particles with the electromagnetic spectrum. Hence, based on the shape, aggregation/agglomeration, the symmetry and size of the nanoparticles Raman peak positions change. This is well understood in the present system as mentioned in Table 2.

Compared to A and C samples of $\text{Sn}_{0.5}\text{Zn}_{0.5}\text{O}_2$, B sample shows a redshift in Raman spectra which is the effect of improved crystallinity of this sample.^[20] Further, the

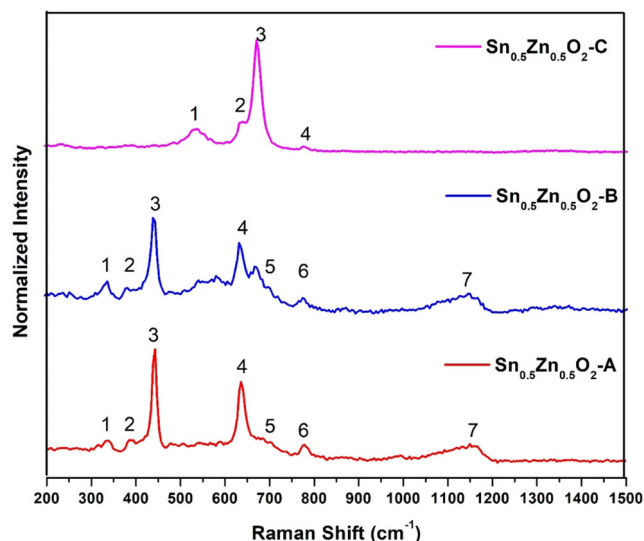


FIGURE 5 Raman analysis of $\text{Sn}_{0.5}\text{Zn}_{0.5}\text{O}_2$ samples

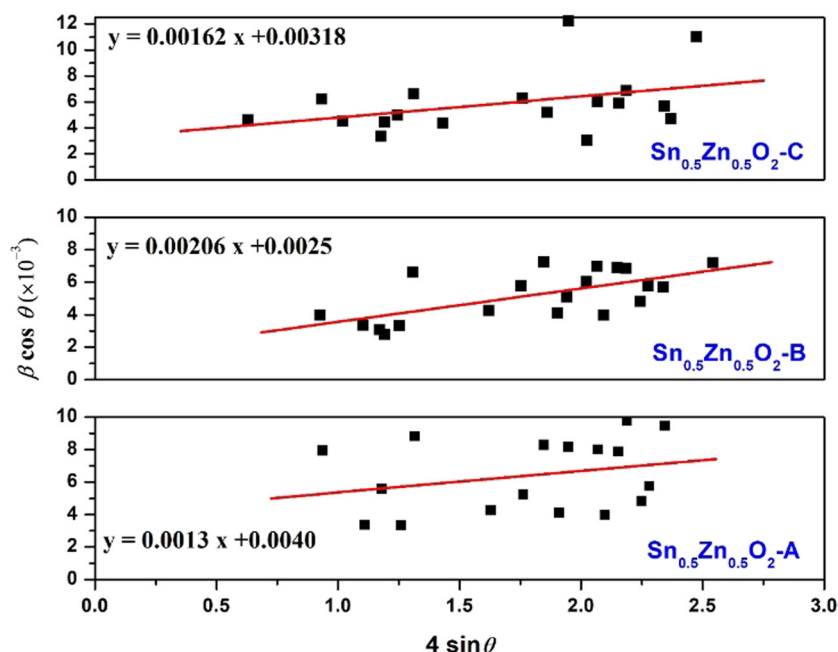


FIGURE 4 WH plot of $\text{Sn}_{0.5}\text{Zn}_{0.5}\text{O}_2$ samples

Peak no	Sn _{0.5} Zn _{0.5} O ₂ -A	Sn _{0.5} Zn _{0.5} O ₂ -B	Sn _{0.5} Zn _{0.5} O ₂ -C	Modes of vibration
1	336.81	335.78	-	E _u
2	388.04	379.90	-	A _{2g}
3	443.19	438.46	-	E _g (SnO ₂)/E ₂ (ZnO)
4	-	-	532.48	B _{1u}
5	635.70	631.76	635.70	A _{1g}
6	673.78	667.74	670.62	A _{2u}
7	776.99	774.88	776.99	B _{2g}

TABLE 2 Raman vibrational modes of Sn_{0.5}Zn_{0.5}O₂ samples

tensile strain also indicates the redshift in the Raman spectra that can be related to the XRD findings discussed in the present research work. Also, Sn_{0.5}Zn_{0.5}O₂ sample of A and C shows higher strain (compressive) in the lattice that reflects in the higher frequency of vibration of these samples. Other than four dominant vibrational modes of SnO₂, other frequencies are also presented around 335 and 670 cm⁻¹. These two peaks can be related to the IR active E_u and A_{2u} modes of transverse optical and longitudinal optical modes of vibrations that are practically Raman forbidden modes. But this is common in the rutile samples calcined below 1000 °C indicating the meager disordered crystal symmetry.^[21,22]

The peak observed at ~532 cm⁻¹ of Sn_{0.5}Zn_{0.5}O₂-C sample is ascribed to the B_{1u} mode is IR active and forbidden mode of Raman.^[23,24] This also can be related to the size decrement/disordered structure/insufficient calcination temperature. But it is found that when choosing NaBH₄ as a reducing agent, treating the Zn_{0.5}Sn_{0.5}O₂ sample below 1000 °C imposes the crystal symmetry disorder compared to the NaOH and LiOH reducing agents. As endnote, almost in all the three samples, the greatest number of the peaks observed in Raman spectra is ascribed to the SnO₂ phase except the peak observed at ~440 cm⁻¹. This peak position matches with the ZnO phase of the E₂ mode of vibration. Hence, the crystal symmetry is not majorly altered either by dopant or changing the reducing agents. Still, increasing the calcination temperature may fix the ordered crystal symmetry in the samples.

3.3 | TEM-SAED analysis

To understand the morphology and planar arrangements of the Sn_{0.5}Zn_{0.5}O₂ samples synthesized by three different reducing agents, TEM analysis is preferred. Figure 6(a–c) represents the Sn_{0.5}Zn_{0.5}O₂ samples prepared by NaOH, LiOH, and NaBH₄, respectively. In Figure 6, SnO₂ particles doped with Zn element prepared by three different reducing agent show mixed geometrical shapes such as

spherical and multi-faceted 3D pyramid morphologies like rectangular, rod shape, and triangular. The variations are marked in the TEM pattern of 100 nm magnification. The clustered TEM image obtained at higher magnification is due to the agglomeration caused by smaller grains. These smaller grains probably appear as spherical distribution throughout the micrograph. From the SAED pattern shown in Figure 6, it is clear that most of the planar arrangements are dominated at (110), (011), and (121) directions. The same has been confirmed by XRD analysis in earlier discussions. Sumanta Sain et al. (2014) mentioned that adoption of preferential direction in planar arrangements (such as rod/pyramid shape) may be the effect of synthesis duration and temperature.^[21] The sample falls in the assorted range of particle sizes starting from 3.5 nm to 9 nm.

Comparatively, the sample synthesized using NaBH₄ reducing agent exhibits more spherical morphology than multifaceted shapes. It can be assumed that the origin of multifaceted shapes emerges from the ZnO phase as identified from the XRD results. The samples synthesized by NaOH and LiOH consist of many numbers of ZnO diffraction planes, whereas the sample prepared by NaBH₄ reducing agent facilitates the SnO₂ phase formation than the former. This is correlated here with respect to the more number of spherical/elongated spherical grains observed in Figure 6c, and hence, based on the common observations, SnO₂ phase results in the spherical morphology. The elemental composition may through more light in this view, which is also presented in the research work.

SAED patterns of samples synthesized by LiOH and NaBH₄ show high intense rings responsible for different miller indices of Sn_{0.5}Zn_{0.5}O₂ samples. The SAED results are more relatable to the XRD results and corresponding hkl planes represented in XRD patterns. Although XRD results exhibit the exterior ZnO phases, from SAED patterns almost all the rings can be indexed with SnO₂ phases. The (011) plane of SnO₂ coincides with the *d*-value of (002) plane of ZnO which is observed at 34° in XRD data. As two peaks observed at ~ 34° belong to

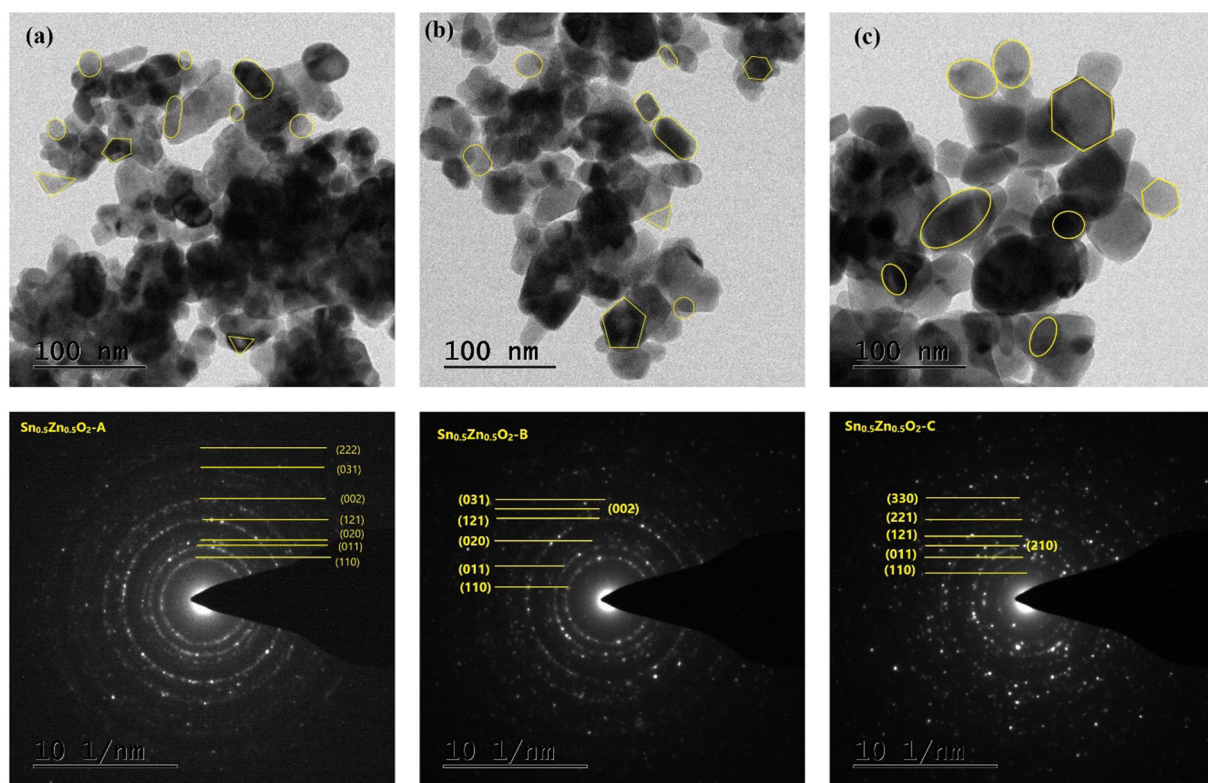


FIGURE 6 TEM micrograph of $\text{Sn}_{0.5}\text{Zn}_{0.5}\text{O}_2$ samples and their SAED patterns

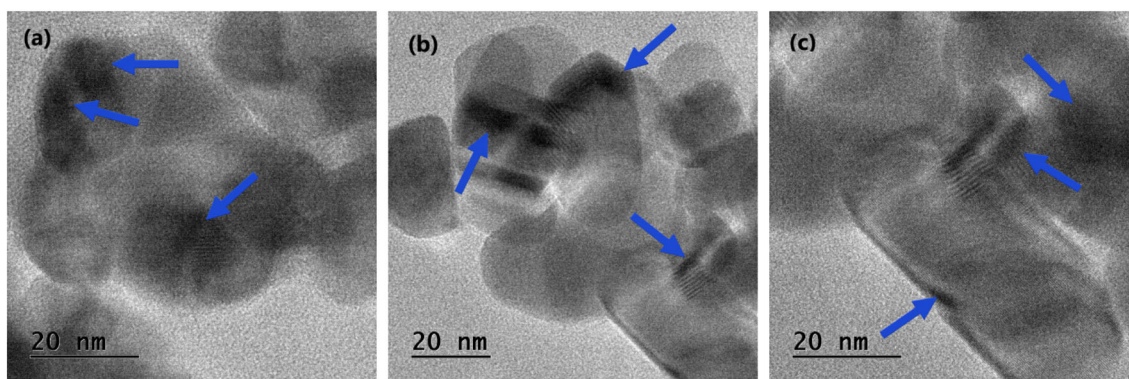


FIGURE 7 TEM micrographs of $\text{Sn}_{0.5}\text{Zn}_{0.5}\text{O}_2$ samples marked with planar dislocations

SnO_2 and ZnO , the appearance of (011) and (002) planes/rings happen together in the SAED pattern. Due to the dominance, only SnO_2 planes are mentioned in the SAED pattern. Overall, SnO_2 phase is primarily seen in both XRD and SAED that indicates the unspoiled crystal symmetry in all three samples prepared by three different reducing agents. However, the presence of lattice imperfections/dislocations is identified in highly magnified images, which are shown in Figure 7. The density of dislocations is calculated and reported in Table 1 from the findings of XRD.

3.4 | EDX analysis

The presence of Sn, Zn, and O elements is confirmed by EDX analysis of all the three samples (Figure 8). The absence of impurities ensures the complete chemical reaction by using NaOH, LiOH, and NaBH_4 reducing agents. All the three samples fall under non-stoichiometry, which is very common in the transition metal compounds. Further, samples exhibit Zn-rich and O-deficit scenarios as seen in Table 3. As discussed in Raman spectra, such deficiency causes lattice imperfections which

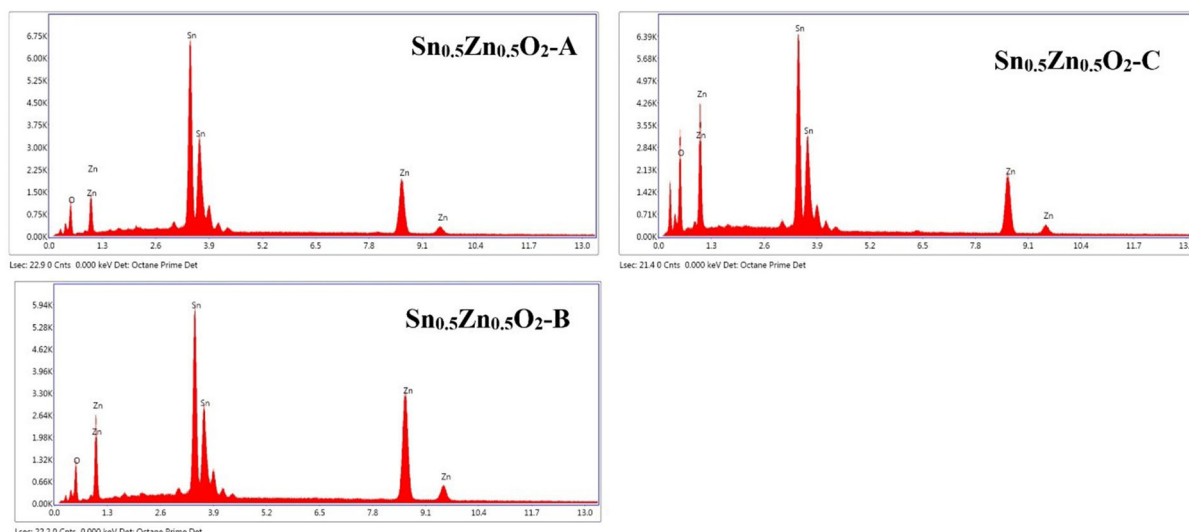


FIGURE 8 EDX analysis of $\text{Sn}_{0.5}\text{Zn}_{0.5}\text{O}_2$ samples

Sample	Atomic weight %			Elemental composition
	Sn	Zn	O	
$\text{Sn}_{0.5}\text{Zn}_{0.5}\text{O}_2\text{-A}$	30.45	41.01	28.54	$\text{Sn}_{0.26}\text{Zn}_{0.63}\text{O}_{1.78}$
$\text{Sn}_{0.5}\text{Zn}_{0.5}\text{O}_2\text{-B}$	31.95	49.25	18.82	$\text{Sn}_{0.27}\text{Zn}_{0.75}\text{O}_{1.17}$
$\text{Sn}_{0.5}\text{Zn}_{0.5}\text{O}_2\text{-C}$	22.53	31.57	45.91	$\text{Sn}_{0.19}\text{Zn}_{0.48}\text{O}_{2.86}$

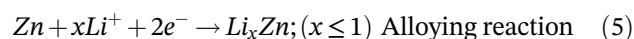
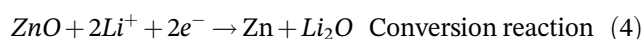
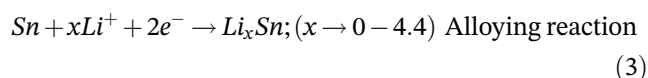
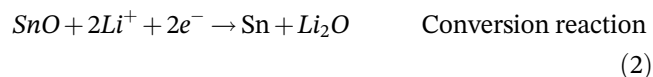
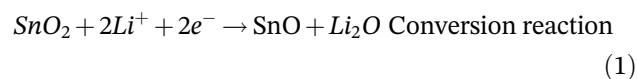
TABLE 3 Elemental composition of $\text{Sn}_{0.5}\text{Zn}_{0.5}\text{O}_2$ samples

can be related to the presence of secondary phases in the XRD pattern. Comparatively, Zn contribution is decreasing in the following order in the Zn-SnO₂ samples: B > A > C, whereas oxygen content follows the order of C > A > B. Tin elemental composition is similar in A and B samples, but C exhibits Sn deficiency compared to these two.

3.5 | Electrochemical analysis

The charge storage properties of Zn doped SnO₂ anode material prepared by NaOH, LiOH, and NaBH₄ are analyzed by CV and galvanostatic charge discharge (GCD), and the findings are presented here. As discussed, the present system consists of two phases—(1) Zn included SnO₂ and (2) ZnO phase—and hence, the electrochemical responses of both of these metal oxides are probable in the present research. SnO₂ and ZnO phases exhibit both pseudocapacitive and Faradaic type redox peaks. Particularly, SnO₂ exhibits three-step redox reactions inclusive of conversion and alloying types, the alloying type redox reaction exhibits Faradaic peaks. But the composition of Sn is an essential factor to view the clear redox peaks of these samples in the CV if obtained.

The CV patterns presented here consist of more than two pairs of redox peaks which may be the collective effect of both SnO₂ and ZnO phases producing redox peaks. The details of redox reactions that SnO₂ and ZnO phases undergo are as follows^[25–28]:



SnO₂ anode material delivers a theoretical capacity of 1494 mAh g⁻¹^[7] at ideal conditions, whereas ZnO delivers a theoretical capacity of 987 mAh g⁻¹.^[15] As mentioned in the above equations, the multi-electron

transfer process consists of Li_2O phase formation. This is an inactive phase and traps lithium source if reactions are not reversed completely. However, measurement conditions, such as choice of electrolyte, solvent, inactive phase formations, chemically-electrochemically irreversible phases, and atmospheric oxygen, play a role in redox peaks and end performance of the active materials.

In the present work, redox peaks are seen at a similar potential for different scan rates almost in all three samples. The samples are tested for a wide potential window -1.0 V to $+1.0$ V vs. Ag/AgCl. Due to the stability issues of aqueous solutions beyond 1.23 V, the CV results consist of H_2 generation and O_2 evolution, which are shown in Figure 9. Here the figure consists of CV responses of $\text{Sn}_{0.5}\text{Zn}_{0.5}\text{O}_2$ samples prepared by NaOH, LiOH, and NaBH_4 in a scan rate of 20 mV s^{-1} . The peak positions observed for all three samples are mentioned in Table 4. The effect of different scan rates on the CV pattern is given in the supporting information section, Figure S1.

Especially, redox peaks observed at lower potential can be ascribed to the Zn^+/Zn redox couple due to the lower reduction potential of this element

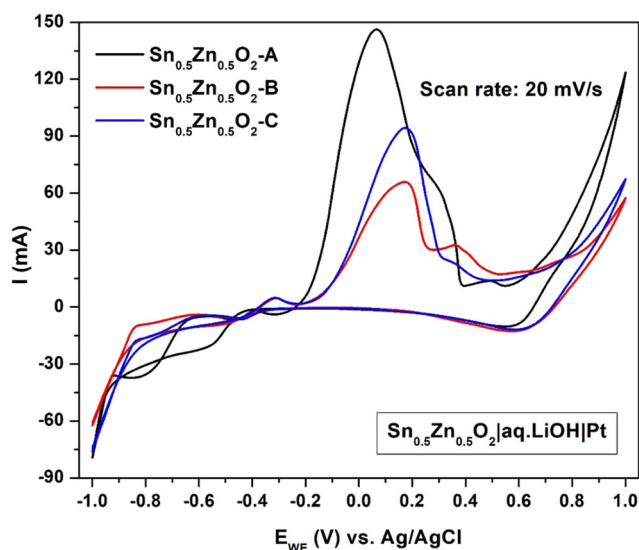


FIGURE 9 Comparative cyclic voltammogram of all the samples

TABLE 4 Peaks potentials obtained in CV of $\text{Sn}_{0.5}\text{Zn}_{0.5}\text{O}_2$ samples

Sample	Peak potential (V vs. Ag/AgCl)					
	Anodic			Cathodic		
$\text{Sn}_{0.5}\text{Zn}_{0.5}\text{O}_2\text{-A}$	-0.3740	0.0691	0.3000	0.5725	-0.5025	-0.8177
$\text{Sn}_{0.5}\text{Zn}_{0.5}\text{O}_2\text{-B}$	-0.3124	0.1397	0.3601	0.5240	-0.4467	-0.8260
$\text{Sn}_{0.5}\text{Zn}_{0.5}\text{O}_2\text{-C}$	-0.3124	0.2007	0.3515	0.5706	-0.4557	-0.8105

(-0.76 V vs. SHE). The redox couple observed at a higher potential ~ 0.2 V can be ascribed to the SnO_2 phase due to its higher standard electrode potential (-0.09 V vs. SHE). Compared to oxidation peaks, the reduction peaks are not very steep which may be due to incomplete intercalation/deintercalation reaction occurring during electrochemical reactions. The peak current values increase in all the samples as the scan rate is increased which indicates the rapid charge carrier migration in accordance with the Nernstian conditions for reversible electrochemical systems, Figure S1. On the other hand, an additional oxidation peak at 0.5 V observed in the $\text{Sn}_{0.5}\text{Zn}_{0.5}\text{O}_2\text{-A}$ sample is unknown which may be the effect of the copper foil electrode. However, this pair is absent in the remaining two samples.

Similarly, cycling tests and columbic efficiencies of the three samples are recorded for 500 cycles at a current density of 1 A g^{-1} and the results are presented in Figure 10. There is not much discrepancy is observed between charging and discharging capacitances of $\text{Sn}_{0.5}\text{Zn}_{0.5}\text{O}_2$ samples. Comparatively, the NaBH_4 sample delivers high capacitance $\sim 250 \text{ mAh g}^{-1}$ whereas $\text{Sn}_{0.5}\text{Zn}_{0.5}\text{O}_2\text{-A}$ and $\text{Sn}_{0.5}\text{Zn}_{0.5}\text{O}_2\text{-B}$ samples deliver $\sim 225 \text{ mAh g}^{-1}$ and $\sim 160 \text{ mAh g}^{-1}$. As seen from other physicochemical studies, sodium-based reducing agents are far good at producing a good amount of charge storage compared to LiOH. Because the reducing power of NaBH_4 and NaOH is better than the LiOH since the B-H and O-H bonds in the former are weaker than the O-H bond in LiOH. Hence more amount of active materials are produced. Also, samples synthesized using Na-based agents possess more SnO_2 phase than the composition of ZnO phase which facilitates the total charging and discharging capacities of the samples. However, the resultant capacity values are very low when compared to the theoretical capacity values of $\text{SnO}_2\text{-ZnO}$ anodes as mentioned above. Again, the present work cannot be directly balanced against with those values due to the analysis conditions. A similar work on SnO_2 anode employing aqueous electrolyte is reported elsewhere.^[29]

Overall, the electrochemical performances of the samples can be sorted in the following order: $\text{C} > \text{A} > \text{B}$. Although peak current and shape of the CV patterns are high in the A sample, as mentioned earlier, excluding the

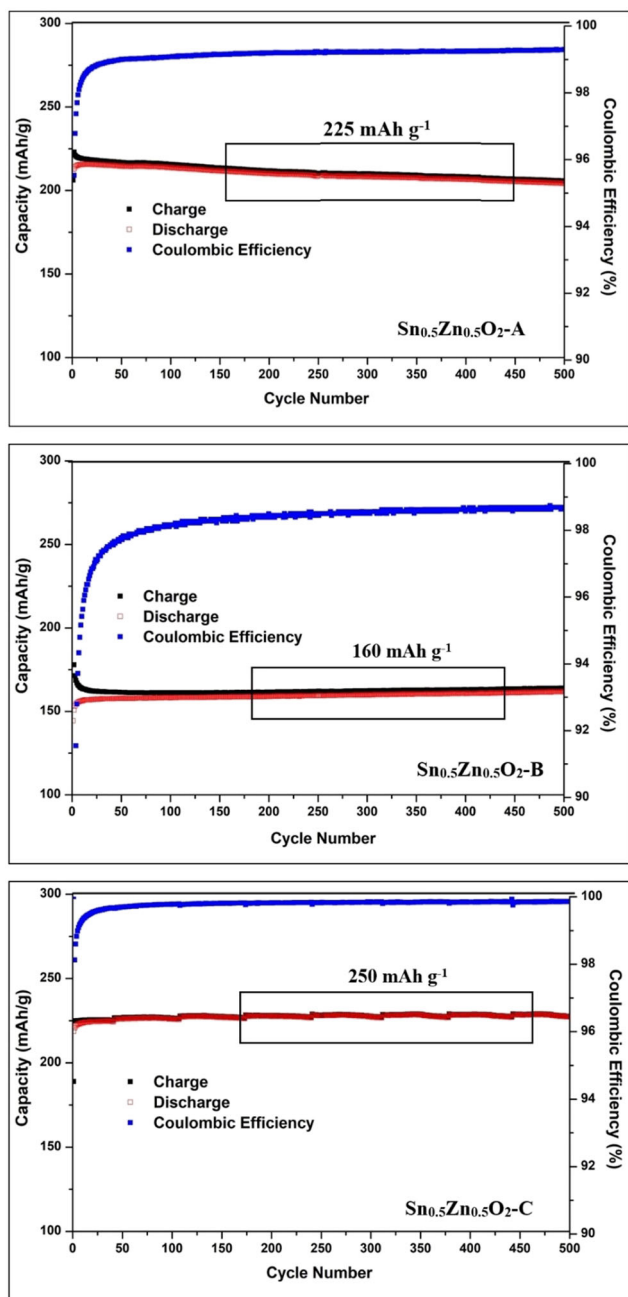


FIGURE 10 Cycling studies of the $\text{Sn}_{0.5}\text{Zn}_{0.5}\text{O}_2$ anodes

substrate effect and optimizing the reversible amount of electrochemical reactions make this sample fall next to the C sample (synthesized using NaBH_4). In the aspects of alkaline mediums during synthesis, NaOH provides greater electrochemical property to the $\text{Sn}_{0.5}\text{Zn}_{0.5}\text{O}_2$ sample than LiOH . This can be due to the high electronegativity of Li which may have formed SnLi/ZnLi alloys resulting in an incomplete $\text{Sn}_{0.5}\text{Zn}_{0.5}\text{O}_2$ phase. However such phases are not seen in XRD possibly due to low trace. Also, the LiOH sample exhibits a higher crystallite size among all three which may inhibit the effective intercalation/deintercalation process of this compound.

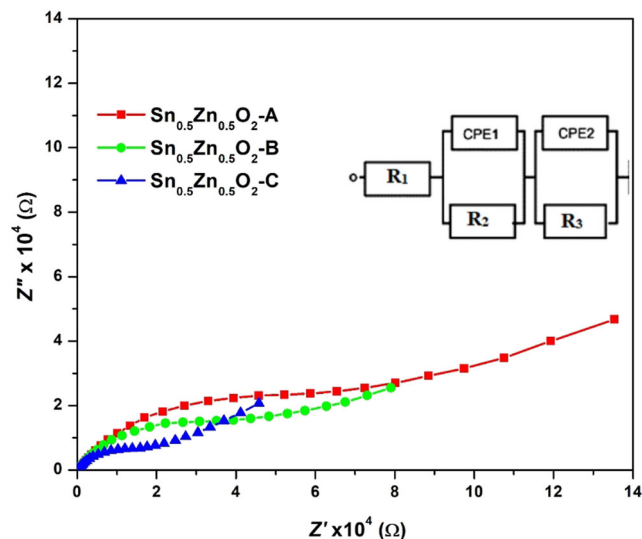


FIGURE 11 Nyquist plot obtained for $\text{Sn}_{0.5}\text{Zn}_{0.5}\text{O}_2$ samples

3.6 | AC impedance analysis

The $\text{Sn}_{0.5}\text{Zn}_{0.5}\text{O}_2$ samples prepared by different reducing agents are analyzed for electrical properties by AC impedance analysis. The response recorded in the frequency range 100 mHz to 100 kHz are presented in Figure 11. Nyquist plots show two depressed semicircles in the higher and lower frequencies respectively. These semicircles indicate the grain and grain boundary effects of the corresponding nanoparticles. The Nyquist plots are fitted through EC-lab software with minimum fitting errors. The resistance values obtained through fitting are given in Table 5.

The electrical conductivity values of the $\text{Sn}_{0.5}\text{Zn}_{0.5}\text{O}_2$ samples are calculated using the Arrhenius equation,²⁸

$$\sigma = 1/RA \text{ (S cm}^{-1}\text{)}$$

where

$\sigma \rightarrow$ electrical conductivity (S cm^{-1}),

$l \rightarrow$ thickness of the pellet (mm),

$A \rightarrow$ area of the pellet (cm^2), and

$R \rightarrow$ resistance (Ω).

The grain resistance values of samples are in the following order: $C < A < B$. The behavior can be attributed to the crystallite sizes of these samples observed in XRD and better elemental composition of C and A sample than that of the B sample. Still, refined interpretations of this behavior need critical measurement in different frequency ranges. A similar scenario is observed for the grain boundary region. Overall, $\text{Sn}_{0.5}\text{Zn}_{0.5}\text{O}_2$ sample

TABLE 5 Resistance and conductivity of $\text{Sn}_{0.5}\text{Zn}_{0.5}\text{O}_2$ samples

Parameters/sample Circuit	$\text{Sn}_{0.5}\text{Zn}_{0.5}\text{O}_2\text{-A}$	$\text{Sn}_{0.5}\text{Zn}_{0.5}\text{O}_2\text{-B}$	$\text{Sn}_{0.5}\text{Zn}_{0.5}\text{O}_2\text{-C}$
	R1 + Q2/R2 + Q3/R3		
R1 (Ω)	8.79	9.61	7.23
R_g (Ω)	13,728	22,806	9133
R_{gb} (Ω)	105,208	100,438	73,753
$\sigma_{\text{Total}} \times 10^{-4}$ (S cm^{-1})	4.94	3.23	7.38

synthesized by NaBH_4 exhibits better electrical conductivity 7.38×10^{-4} (S cm^{-1}) than the other two samples. Sample A falls next to C with a conductivity value of 4.94×10^{-4} (S cm^{-1}), whereas sample B shows 3.22×10^{-4} (S cm^{-1}). This pattern of electrical behavior is comparable to the findings of other analyses discussed throughout this research work. Further, the present values of electrical conductivity of the $\text{SnO}_2\text{-ZnO}$ composite are higher than their individual entities as reported widely.^[30,31]

4 | CONCLUSIONS

The mutual dependency of synthesis medium and physicochemical-electrochemical properties of $\text{Sn}_{0.5}\text{Zn}_{0.5}\text{O}_2$ is analyzed with respect to NaOH , LiOH , and NaBH_4 reducing agents. The samples are extensively analyzed by XRD, Raman, FESEM-TEM-EDX analysis, CV-GCD, and AC impedance analysis. The crystallite sizes of the samples prepared using Na-based agents are smaller than the LiOH agent. The morphological pattern reveals assorted yet no aggregated distribution of grains. Mixed symmetry is observed in all three samples as confirmed by SAED and XRD patterns. It is observed that the sample synthesized by NaBH_4 is the best at charge storage properties of Li where $\text{Sn}_{0.5}\text{Zn}_{0.5}\text{O}_2$ by NaOH falls into the next best. Again, the LiOH sample is the least among all as Li_2O phase formation is highly probable in this case and loss of active metal composition as passive phase is the limitation in this particular case. Next, NaBH_4 samples deliver the highest electrical conductivity, 7.38×10^{-4} S cm^{-1} , compared to the other two at room temperature. Finally, among the chosen basic reducing agents, Na-based agents are better at reducing the Sn-Zn chlorides than the LiOH since the bonding between B-H and O-H is weaker in Na-containing salts than LiOH .

ACKNOWLEDGMENTS


Dr. D. Lakshmi acknowledges CSIR, Government of India for the financial assistance through research associateship [09/472(0189)/219-EMR-I].

AUTHOR CONTRIBUTIONS

Devaraj Lakshmi: Conceptualization; investigation. **M. Infanta Diana:** Methodology; resources. **Gayathri Manoj:** Methodology. **Balakrishnan Nalini:** Formal analysis; supervision. **P. Balraju:** Resources.

ORCID


D. Lakshmi  <https://orcid.org/0000-0001-7176-8007>

M. Infanta Diana  <https://orcid.org/0000-0002-7075-9675>

Gayathri Manoj  <https://orcid.org/0000-0001-6007-6910>

S. Jayapandi  <https://orcid.org/0000-0003-3602-8374>

B. Nalini  <https://orcid.org/0000-0002-7615-0529>

P. Christopher Selvin  <https://orcid.org/0000-0002-3354-5790>

P. Balraju  <https://orcid.org/0000-0001-9519-6955>

REFERENCES

- [1] J. He, A. Bhargav, A. Manthiram, *ACS Nano* **2021**, *15*, 8583.
- [2] Y. Yang, W. Fu, D. C. Lee, C. Bell, M. Drexler, Z. F. Ma, A. Magasinski, G. Yushin, F. M. Alamgir, *Mater. Today Energy* **2020**, *16*, 100410.
- [3] K. N. Dinh, Q. Liang, C.-F. Du, J. Zhao, A. I. Y. Tok, H. Mao, Q. Yan, *Nano Today* **2019**, *25*, 99.
- [4] N. Nitta, F. Wu, J. T. Lee, G. Yushin, *Mater. Today* **2015**, *5*, 252.
- [5] J. Ma, Y. Kong, S. Liu, Y. Li, J. Jiang, Q. Zhou, Y. Huang, S. Han, *ACS Appl. Energy Mater.* **2020**, *3*, 11900.
- [6] L. Yu, J. Liu, X. Xu, L. Zhang, R. Hu, J. Liu, L. Yang, M. Zhu, *ACS Appl. Mater. Interfaces* **2017**, *3*, 2516.
- [7] R. Hu, Y. Ouyang, T. Liang, H. Wang, J. Liu, J. Chen, C. Yang, L. Yang, M. Zhu, *Adv. Mater.* **2017**, *29*, 1605006.
- [8] Z. Huang, H. Gao, Z. Yang, W. Jiang, Q. Wang, S. Wang, J. Ju, Y.-U. Kwon, Y. Zhao, *Mater. Des.* **2019**, *180*, 107973.
- [9] Y. Cheng, A. Nie, L.-Y. Gan, Q. Zhang, U. Schwingenschlöggl, *J. Mater. Chem. A* **2015**, *3*, 19483.
- [10] M. K. Kim, W. H. Shin, H. M. Jeong, *Appl. Surf. Sci.* **2019**, *467–468*, 926.
- [11] P. Li, K. Zhang, J. H. Park, *J. Mater. Chem. A* **2018**, *6*, 1900.
- [12] J. Zhang, L. Li, J. Chen, N. He, K. Yu, C. Liang, *J. Phys. Chem. Solids* **2021**, *150*, 109861.
- [13] M. Ahmad, S. Yingying, H. Sun, W. Shen, J. Zhu, *J. Solid State Chem.* **2012**, *196*, 326.
- [14] Y. Zhao, X. Li, L. Dong, B. Yan, H. Shan, D. Li, X. Sun, *Int. J. Hydrogen Energy* **2015**, *40*, 14338.

- [15] L. Luo, W. Xu, Z. Xia, Y. Fei, J. Zhu, C. Chen, Y. Lu, Q. Wei, H. Qiao, X. Zhang, *Ceram. Int.* **2016**, *42*, 10826.
- [16] A. Yaghtin, S. M. Masoudpanah, M. Hasheminasari, A. Salehi, D. Safanama, C. K. Ong, S. Adams, M. V. Reddy, *Molecules* **2020**, *25*, 3746.
- [17] S. Jayapandi, S. Premkumar, D. Lakshmi, P. Packiyaraj, K. B. Viswanath, P. Sivaraj, K. Anitha, *Electron.* **2019**, *30*, 8479.
- [18] D. Lakshmi, B. Nalini, *J. Solid State Electrochem.* **2017**, *21*, 1027.
- [19] A. Kar, M. A. Stroschio, M. Dutta, J. Kumari, M. Meyyappan, *Semicond. Sci. Technol.* **2010**, *25*, 024012.
- [20] D. Lakshmi, M. I. Diana, B. Nalini, G. G. Soundarya, P. Priyanka, S. Jayapandi, P. C. Selvin, *J. Mater. Sci.: Mater. Electron.* **2021**, *32*, 27384.
- [21] S. Sain, A. Kar, A. Patra, S. K. Pradhan, *Cryst. Eng. Comm.* **2014**, *16*, 1079.
- [22] S. H. Sun, G. W. Meng, G. X. Zhang, T. Gao, B. Y. Geng, L. D. Zhang, J. Zuo, *Chem. Phys. Lett.* **2003**, *376*, 103.
- [23] A. Diéguez, A. Romano-Rodríguez, A. Vilà, J. R. Morante, *Appl. Phys. Rev.* **2001**, *90*, 1550.
- [24] I. M. Costa, Y. N. Colmenares, P. S. Pizani, E. R. Leite, A. J. Chiquito, *Chem. Phys. Lett.* **2018**, *695*, 125.
- [25] Y. Chen, M. He, N. Zhao, J. Fu, H. Huo, T. Zhang, Y. Li, F. Xu, X. Guo, *J. Power Sources* **2019**, *420*, 15.
- [26] X. W. Guo, X. P. Fang, Y. Sun, L. Y. Shen, Z. X. Wang, L. Q. Chen, *J. Power Sources* **2012**, *226*, 75.
- [27] L. Lei, X. Wenzheng, X. Zhaokang, F. Yaqian, Z. Jiadeng, C. Chen, L. Yao, W. Qufu, Q. Hui, Z. Xiangwu, *Ceram. Int.* **2016**, *42*, 10826.
- [28] Y.-N. Zhou, W.-J. Li, Z.-W. Fu, *Electrochim. Acta* **2011**, *59*, 435.
- [29] D. V. Raj, N. Ponpandian, D. Mangalaraj, C. Viswanathan, *Mater. Sci. Semicond. Process.* **2014**, *26*, 55.
- [30] M. Caglar, S. I., Y. Caglar, F. Yakuphanoglu, *Appl. Surf. Sci.* **2009**, *255*, 4491.
- [31] A. Zanka, K. Gadani, V. Vadgama, B. Udeshi, M. Gal, S. Solanki, A. Vaishnani, V. G. Shrimali, P. S. Solanki, N. A. Shah, D. D. Pandya, *Phys. B* **2021**, *617*, 413140.

SUPPORTING INFORMATION

Additional supporting information may be found in the online version of the article at the publisher's website.

How to cite this article: D. Lakshmi, M. I. Diana, G. Manoj, S. Jayapandi, B. Nalini, P. C. Selvin, P. Balraju, *Appl Organomet Chem* **2022**, e6714.
<https://doi.org/10.1002/aoc.6714>